Geochemistry Geophysics Geosystems G3

Article
Volume 12, Number 3
30 March 2011
Q03014, doi:10.1029/2010GC003413
ISSN: 1525-2027

Published by AGU and the Geochemical Society

Microsegregation rates of liquid Fe-Ni-S metal in natural silicate-metal systems: A combined experimental and numerical study

Tracy Rushmer

Department of Earth and Planetary Sciences, GEMOC, Macquarie University, North Ryde, NSW 2109, Australia (tracy.rushmer@mq.edu.au)

Nick Petford

University of Northampton, Park Campus, Northampton NN2 7AL, UK

Also at Department of Earth and Planetary Sciences, GEMOC, Macquarie University, North Ryde, NSW 2109, Australia

[1] We present results of an image-based numerical model aimed at quantifying the microsegregation and flow of liquid metal in meteorites prior to the onset of silicate melting. The sample material is the H6 chondrite Kernouvé. The model utilizes the observed geometry of two distinct chondrite textures associated with grain-scale melt segregation in the following: (1) the undeformed (natural) state and (2) during deformation and partial melting under controlled (laboratory) conditions. The numerical simulations recover liquid metal segregation rates of ~10^{-6} to 10^{-4} m s^{-1} for matrix permeabilities (k) of $10^{-12} < k < 10^{-10}$ m^2 and pressure gradients of ~1 and 10^4 Pa m^{-1}. The velocity flow field is position-dependent across the sample, reflecting initial grain-scale heterogeneity and anisotropy in the spatial distribution of metal prior to melting. In addition to porous flow, we use a coupled Brinkman-Navier-Stokes solution to quantify liquid metal segregation through deformation-induced microscale veins. Melt flow velocities in veins are several orders faster than matrix flow, implying that a combination of porous (grain-scale) flow feeding into a network of small-scale cracks and veins during the initial stages of partial melting may be an extremely efficient mechanism for segregating liquid metal from silicate matrix in planetesimals undergoing deformation. This mechanism may be temporary and confined only to the earliest stages of melt microsegregation because with increasing temperature, the onset of silicate melting shuts off liquid metal segregation by creeping matrix flow. The point at which this occurs marks an important transition in the mode and style of internal differentiation.

Components: 6800 words, 13 figures, 2 tables.

Keywords: core formation; planetesimal; experiment; numerical simulations; partial melting.

Index Terms: 5455 Planetary Sciences: Solid Surface Planets: Origin and evolution; 3225 Mathematical Geophysics: Numerical approximations and analysis (4260); 3630 Mineralogy and Petrology: Experimental mineralogy and petrology.

Received 20 October 2010; **Revised** 14 January 2011; **Accepted** 18 February 2011; **Published** 30 March 2011.

Rushmer, T., and N. Petford (2011), Microsegregation rates of liquid Fe-Ni-S metal in natural silicate-metal systems: A combined experimental and numerical study, *Geochem. Geophys. Geosyst.*, *12*, Q03014, doi:10.1029/2010GC003413.

1. Introduction

[2] Our understanding the rates of differentiation in silicate bodies comprising the early solar system is based almost exclusively on results from studies using short-lived radioisotopes [*Lee and Halliday*, 1996; *Harper and Jacobsen*, 1996; *Yin et al.*, 2002; *Kleine et al.*, 2002, 2005; *Carlson and Boyet*, 2009]. The fine temporal resolution provided by these isotopic systems show that planetary differentiation must have started very early and proceeded quickly [*Kleine et al.*, 2009]. The strongest evidence for this comes from the low $^{182}W/^{184}W$ ratios in magmatic iron meteorites. Magmatic irons have long thought to be representative of planetesimal cores and thus knowing their age provides insight into the rates of early solar system differentiation processes. *Kelly and Wasserburg* [1978] used the decay of ^{107}Pd to ^{107}Ag (half-life 6.5 Myr) to suggest that magmatic irons formed within ~15 Myr of the start of the solar system, a result apparently confirmed by *Lee and Halliday* [1995] using ^{182}Hf-^{182}W chronometry. Within the last 5 years, significant advances using the $^{182}W/^{184}W$ system points to a convergence in ages of magmatic irons with Calcium Aluminum Inclusions (CAIs), thought to represent the first solids to have condensed in the solar nebula [*Kleine et al.*, 2005; *Burkhardt et al.*, 2008]. *Lee* [2005] suggested that metal-silicate segregation occurred within the first 1–3 Myr after the formation of the solar system but did not consider the cosmogenic effects on W isotopes. This timing is likely too long because the spread in ages may be solely due to the unaccounted effects. When considering cosmogenic effects, *Klein et al.* [2005] found that irons must have formed within ~1.5 Myr of CAI material. Additional studies by *Quitté et al.* [2006] using the ^{60}Fe-^{60}Ni system and *Markowski et al.* [2006] imply that some irons formed within a few hundred thousand years of the start of the solar system. *Qin et al.* [2008] also found accretion and core formation of planetesimals occurred very early (~1.5 Myr). The sum of these isotopic studies is that the age of magmatic irons now appears virtually indistinguishable from the age of CAIs and of the solar system itself [*Kleine et al.*, 2009; *Carlson and Boyet*, 2009].

[3] In summary these geochemical results demand a physical mechanism for liquid metal-silicate segregation and core formation that is both rapid and efficient. This has long been recognized [*Stevenson*, 1981] who evoked diapirism as the most plausible segregation mechanism over large length scales. But in recent years arguments in favor of percolation and deformation-driven flow have gained some level of acceptability [e.g., *Bruhn et al.*, 2000; *Rushmer et al.*, 2000, 2002, 2005; *Yoshino et al.*, 2003, 2004]. In particular, *Rushmer et al.* [2005] looked at the role of shear-induced segregation in planetseimals set up in response to external perturbations via impacts as a mechanism for core formation.

[4] In this present study we build on previous experimental work by *Rushmer et al.* [2000, 2005] on the Kernouvé H6 chondrite. *Rushmer et al.* [2005] describes the KM experiments in detail, including the deformation sample KM-24 used in this study. In order to provide a more robust analysis of the possible range of metallic liquid migration velocities, our numerical approach in this study takes advantage of the observed texture before (the natural Kernouvé H6 chondrite) and after deformation (experiment KM-24) as the template for the finite element fluid flow models. In attempting to further constrain the possible rates of liquid metal-silicate segregation using numerical modeling we hope to reconcile the physics of the segregation process with timescales based on isotopic analysis.

2. Metallic Liquid-Silicate Matrix Microsegragation

2.1. Previous Studies

[5] The physical mechanisms responsible for segregation of liquid metal from silicate matrix, a critical precursor for core formation, have become less obscure and arguably less contentious, at least for segregation on small length scales. In several recent papers, it has been shown that percolative flow of FeS alloys in a silicate matrix is in fact possible despite long-standing arguments against based on surface tension effects [e.g., *Minarik et al.*, 1996; *Shannon and Agee*, 1996; *Ballhaus and Ellis*, 1996]. In particular, two papers by *Yoshino et al.* [2003, 2004] showed experimentally that melt connectivity exists where the FeS melt fraction is ~6%–10% provided no silicate melt is present. From this it was argued that planetesimals with radii greater than ~30 km (the minimum size necessary to retain heat from short-lived radioactive nuclei such as ^{26}Al) may already have formed protocores before accreting to form the larger planetesimals and ultimately terrestrial planets. *Rushmer et al.* [2000], *Bruhn et al.* [2000] and *Groebner and Kohlstedt* [2006] have all shown experimentally that deformation plays a pivotal enabling role in the segregation process. Textures found in the Kernouvé experiments showed evidence of migration of liquid

Table 1. The Kernouvé Bulk Composition Along With an Average of Five Other H6 Chondrite Falls From *Jarosewich* [1990][a]

Element	Kernouvé	Average H6 Chondrites
SiO_2	36.31	36.76
TiO_2	0.13	0.13
Al_2O_3	2.31	2.05
Cr_2O_3	0.57	0.54
FeO	9.00	10.21
MnO	0.31	0.34
MgO	23.23	23.42
CaO	1.74	1.82
Na_2O	0.91	0.90
K_2O	0.08	0.09
P_2O_5	0.19	0.28
H_2O+	0.10	0.1–0.5
Fe metal	19.40	15.95
Ni	1.70	1.72
Co	0.08	0.03
FeS	3.74	5.55
C	0.10	0.04
Total	99.90	99.93

[a]The bulk chemistry shows that the Kernouvé is quite comparable to the other H6 chondrite falls, except for higher Fe metal contents and slightly lower FeS contents. Note that there is a range of H_2O+ values given for all the H6 chondrites.

metal liquid during shear along with remobilization of Fe-Ni metal in high strain zones [*Rushmer et al.*, 2000, 2005]. The Kernouvé experiments in these studies indicate that liquid metal can interconnect during deformation in a solid silicate matrix, but the mechanisms will vary depending on external conditions.

[6] In summary, a growing body of evidence points toward flow through a porous silicate framework as the dominant liquid metal microsegregation mechanism, at least during the initial stages of partial melting. We now investigate this possibility further, beginning with a description of the Kernouvé starting material, followed by the results of image-based numerical simulations that attempt to quantify more fully the fluid dynamics of microsegregation.

2.2. Kernouvé (H6 Ordinary Chondrite)

[7] The Kernouvé ordinary chondrite fell on 22 May 1869 near Kernouvé in Morbihan, France. Analysis by *Jarosewich* [1990] confirmed a mineralogy comprising olivine, orthopyroxene, clinopyroxene, plagioclase, chromite and chlorapatite, and, importantly for this study, varying ratios of Fe-Ni-S (Table 1). Kernouvé records a peak shock pressure <5 GPa [*Stoeffler*, 1991] with no oxidation of metal or sulphide [*Wlotzka*, 1993], consistent with fresh (witnessed) falls subjected to little weathering.

[8] While ordinary chondrites have not been melted, H6 chondrites have been subjected to temperatures in the region of ~900°C presumably through metamorphism on their parent body. From chromite-plagioclase assemblages in Kernouvé and the presence Fe-Ni veins, *Rubin* [2003] concluded that shock events could have provided the heat needed to metamorphose Kernouvé. However, *Kleine et al.* [2008] have recently shown that metamorphism of

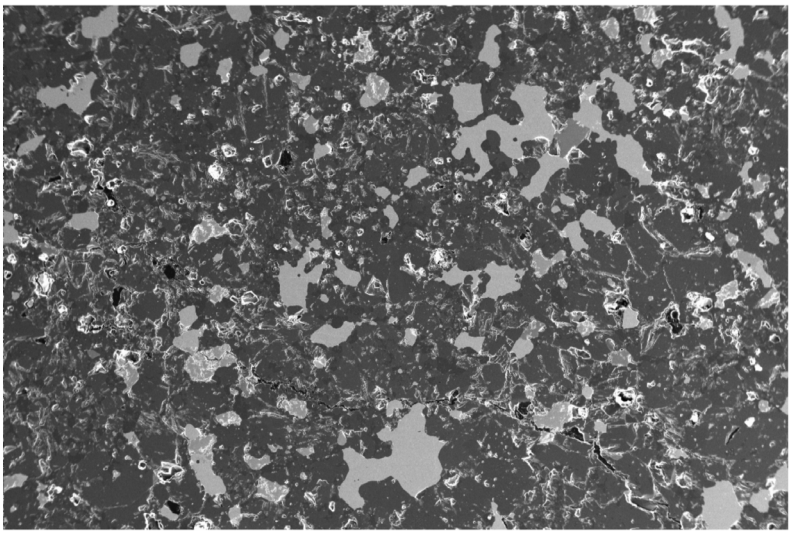

Figure 1. SEM image of Kernouvé texture in natural (undeformed and not experimentally produced) state showing initial distribution of light gray Fe-Ni and Fe-S metal pockets. The silicate matrix comprises olivine, pyroxene, and plagioclase. Image dimension is 8 × 12 mm.

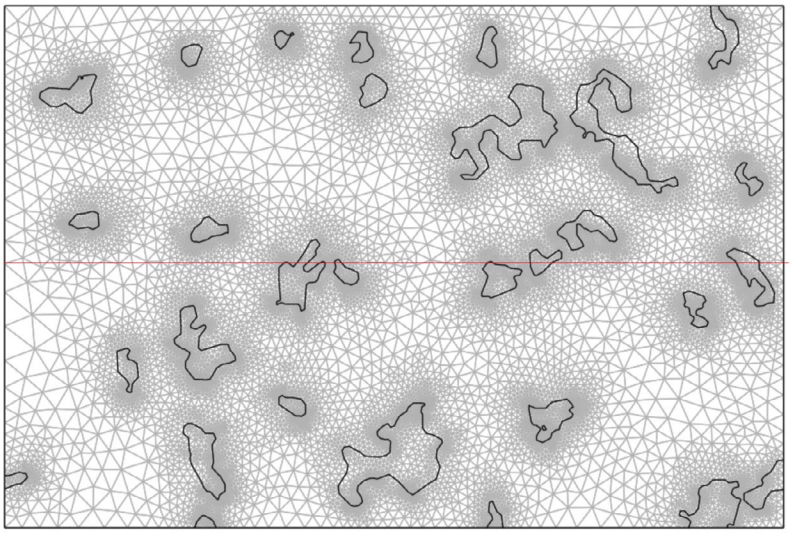

Figure 2. Image-based finite element mesh (22,681 elements) generated from the 2-D texture geometry in Figure 1 at same spatial dimension. Regions of solid FeS metal (light gray areas in Figure 1) are delineated in the numerical flow model as discrete subdomains with assigned liquid metal properties (Table 1). Matrix flow is solved using a Darcy Law approximation for a permeability interval $10^{-12} < k\ 10^{-10}$ m^2 and an initial porosity (melt fraction of 0.1). Red line shows sample midpoint, a useful reference line for calculating position-dependent liquid metal flow velocities in the matrix (see Figure 6).

H chondrite parent body also includes, or can be solely due to, heating from ^{26}Al. Figure 1 shows an SEM image of the natural, well-equilibrated texture common for H6 chondrites.

3. Liquid Metal Microsegragation: Numerical Approach

[9] In order to get a better feel for the possible range in melt migration velocities in partially molten chondrites we have undertaken a series of numerical experiments that attempt to capture metal liquid flow rates through a porous silicate matrix. Two scenarios are envisioned, one where flow takes place by steady state percolation and another where shearing has opened up cracks or dilatant fissures in the silicate matrix. To do this we use as starting geometries the actual textures preserved in the Kernouvé meteorite in its natural state (Figure 1) and after deformation in the laboratory. Specifically we are interested in recovering the liquid metal flow rates through robust application of momentum equations to corroborate (or otherwise) the limited results from previous studies [e.g., *Yoshino et al.*, 2004], and to assess the relative difference in flow rates as a function of the microsegregation process itself. Qualitatively, although fracture (channel) flow should be faster than porous (or percolative) flow, it is prudent nonetheless to confirm this through quantitative analysis. The end result is to gain further insight into the rates of microphysics of segregation as a precursor to larger-scale transport mechanisms thought to be important in planetary core formation.

[10] The numerical part has been done by solving the fluid flow equations using the actual rock texture as a template. This 2-D image-based modeling approach exploits the capability of the Finite Element software (Comsol Multiphysics) to use real object geometry as the basis for the finite element mesh [*Petford et al.*, 2006]. The model is set up by exploiting a feature of Comsol that allows users to import SEM gray scale images (e.g., Figure 1) via an in-house Matlab script to construct a bespoke numerical simulation. The advantage of this methodology is that the numerical results (2-D fluid flow field, pressure distribution) can be compared directly with the rock texture in both the natural (undeformed state) and that resulting from laboratory deformation. The numerical models can thus be cross-referenced with the true textures and geometry that define uniquely the sample material under investigation (Figure 2). Image-based modeling is being used increasingly in applications where the numerical outcome is governed by the detailed internal structure of the material under investigation [e.g., *Chen et al.*, 2004; *Xiaobin Shen et al.*, 2007].

Table 2. Variables, Units, and Physical Properties Used in the Models

Symbol	Unit/Value	Meaning	Reference
k	$10^{-12} < k < 10^{-10}$ m s^{-1}	Matrix permeability	*Yoshino et al.* [2003]
g	0.1 m s^{-2}	Acceleration due to gravity	*Yoshino et al.* [2003] based on planetesimal radius r = 100 km
ρ	7000 kg m^{-3}	Liquid metal alloy (melt) density	*Secco et al.* [1998]
η	$10^{-3} < \eta < 10^{-2}$ Pa s	Liquid metal alloy (melt) viscosity	*Terasaki et al.* [2001]
r	100 km	Planetesimal radius	*Yoshino et al.* [2003]
f	0.1–0.4	Melt fraction (Fe-Ni-S) liquid metal	*Rushmer et al.* [2000, 2005]
Pa m^{-1}	1.25, 1.125 × 10^4	Assumed pressure gradient driving fluid flow	This study

[11] Once a mesh has been created at the desired resolution (Figure 2), appropriate boundary conditions can be applied. These are the following: (1) walls (no slip), (2) upper boundary (inlet pressure), and (3) lower boundary (outlet pressure). According to *Stevenson* [1989], pockets of melt within a solid matrix define regions of low pressure and low viscosity that will attract melt toward them and also help localize deformation. To test this idea we have set the boundaries between the regions of Fe-S and Fe-Ni metal (e.g., Figure 1) and surrounding silicate matrix as continuous (boundary condition 4), meaning that during the simulation, percolating liquid metal is free to move between matrix and melt pools defined as early sites of partial melting. Other more restrictive boundary conditions are of course permitted but have not been investigated in this instance. See Table 2 for a list of physical parameters and other model variables.

[12] The initial conditions relate to the fluid transport properties, that is, density and viscosity of the Fe-Ni-S melt, the gravity field and the matrix permeability. The latter is not known for Kernouvé, but *Yoshino et al.* [2004] report values of 10^{-11} to 10^{-9} m^2 based on their study of olivine and a

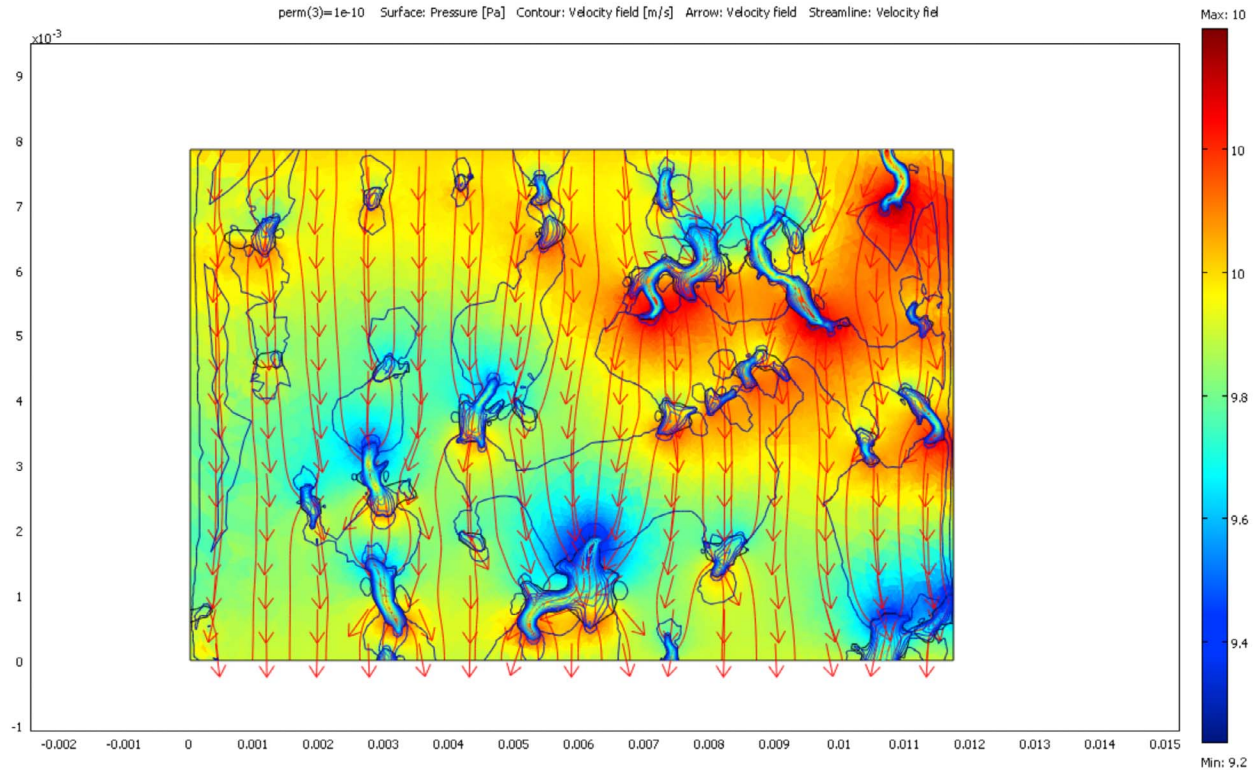

Figure 3. Plot showing numerically generated 2-D surface pressure and fluid flow trajectories (arrows) for image shown in Figure 1 for a fixed matrix permeability of 10^{-10} m^2. The predicted range in melt flow velocities where liquid metal is free to move downward (segregate) under gravity is of the order 10^{-6} to 10^{-4} m s^{-1}. Melt density is 7000 kg m^{-3}, and matrix porosity (melt fraction) is 0.1. Pressure gradient is 1.25 Pa m^{-1}.

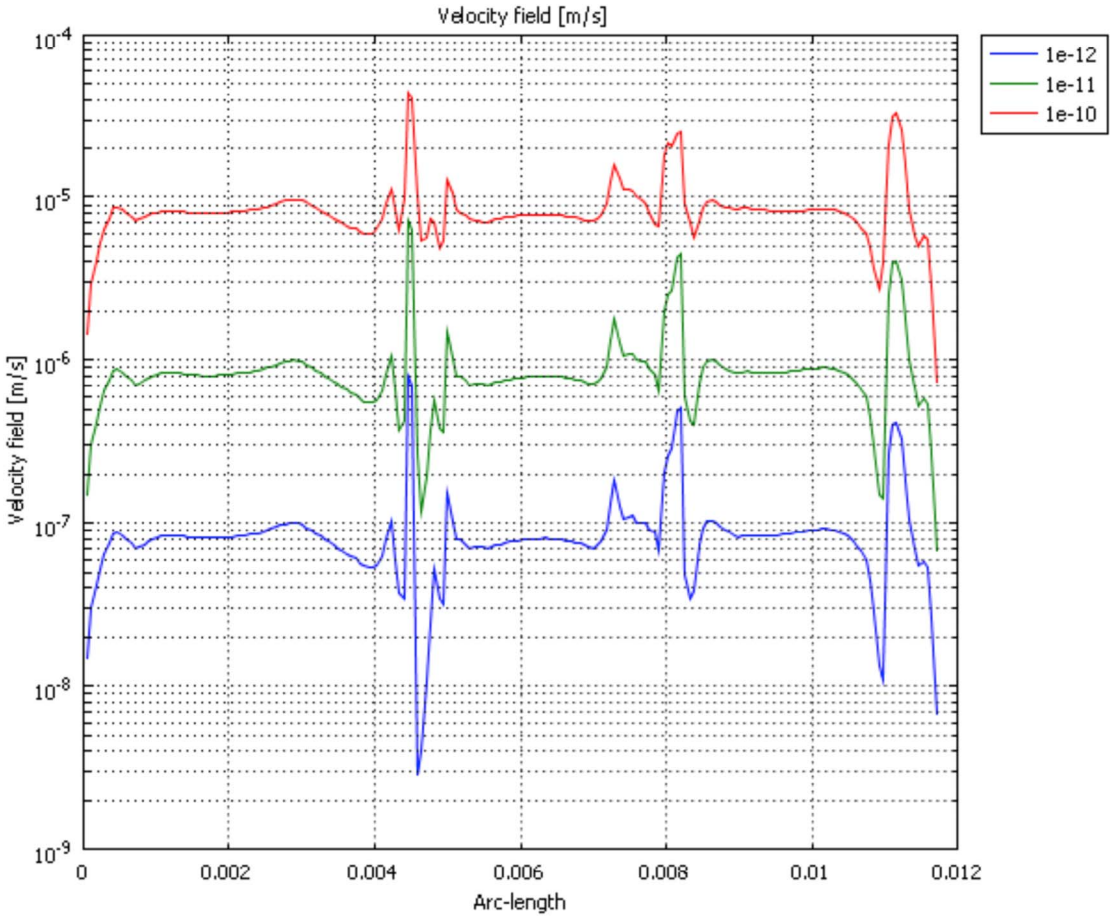

Figure 4. Predicted liquid metal melt flow velocities (m s^{-1}) at the sample image midpoint (red line in Figure 2) for three matrix permeabilities of 10^{-12}, 10^{-11}, and 10^{-10} m^2. Highest matrix flow velocities (~10^{-5} m s^{-1}) correspond to highest matrix permeabilities. The velocity field is position dependent with flow rates governed by matrix texture and structure. Pressure gradient is 1.25 Pa m^{-1}.

sulfide liquid metal melt fraction of 10%. In order to cross-reference our results with theirs, and in the absence of any specific measurements on similar material, we have chosen a complementary range of values in our models of $10^{-12} < k < 10^{-10}$ m^2. These matrix permeabilities are also similar to those published by *Roberts et al.* [2007], but we note the results of a recent study by *Bagdassarov et al.* [2009]. They reported much lower matrix permeability values of 10^{-18} to 10^{-19} m^2 and suggest the earlier studies may not have achieved textural equilibrium. As yet this is still a point of open debate. We discuss the role of matrix permeability in section 4.1. Less problematically, the physical properties of liquid metal alloy are fairly well constrained by experiment [e.g., *Secco et al.*, 1998] and a range of values for both viscosity and density of liquid Fe as a function of temperature, pressure and composition are available. Liquid metal viscosity displays an Arrhenian dependence on temperature [*Terasaki et al.*, 2001] and both its viscosity and density decrease with increasing wt % sulfur [*Secco et al.*, 1998]. Together these factors point to a liquid viscosity (η) in the range $10^{-3} < \eta < 10^{-2}$ Pa s. As we are modeling melt segregation in meteorites whose parent bodies are larger planetesimals or asteroids, we assume an arbitrary body dimension of 100 km where $g = 0.1$ m s^{-2} [see also *Yoshino et al.*, 2004] and a low-pressure melt density of 7000 kg m^{-3}.

[13] We turn now to the numerical model itself. We have employed solution schemes appropriate to the problem in hand. Thus, for the natural, undeformed texture we assume simple (incompressible) Darcian flow with pressure as the dependent variable. The situation is slightly different in the deformed geometry and we solve for fluid flow using the Brinkman equation for the permeable matrix that takes into

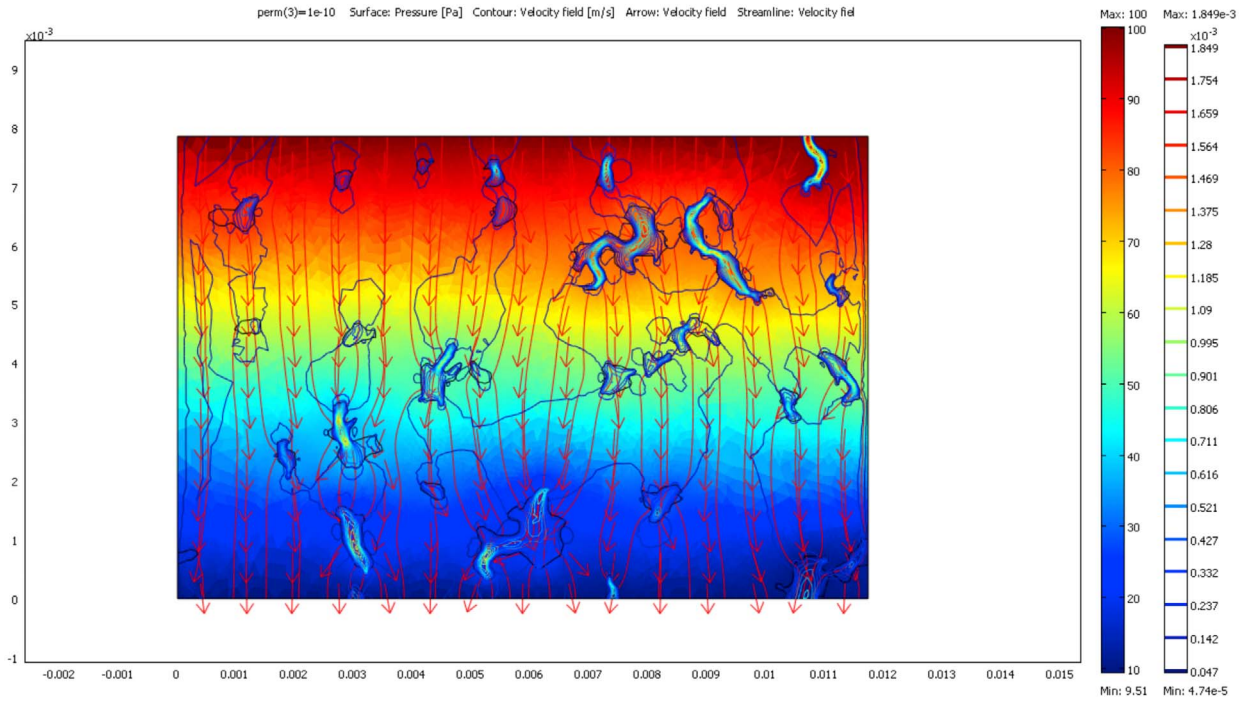

Figure 5. Pressure surface plot for undeformed geometry as in Figure 3 but for a pressure gradient of 1.125×10^4 Pa m^{-1}. Melt velocity ranges from 10^{-3} to 10^{-5} m s^{-1}.

account viscous stresses as melt approaches a wider channel, coupled with a full (viscosity-dependent) Navier-Stokes solution for fluid flow in the vein.

[14] The biggest unknown is the size of the pressure gradient that, along with negative buoyancy, drives the flow of liquid metal. The assumed size of the parent bodies (diameters $\ll$1000 km) and low gravity field point to a low-pressure ambient environment. We thus choose two estimates of pressure gradient that bracket each model within bounds we regard as reasonable: a low (relative) value of 1.25 Pa m^{-1} and a higher value of 1.125×10^4 Pa m^{-1} (for comparison the lithostatic gradient in the earth for rock density of 2800 kg m^{-3} is ~2.7×10^4 Pa m^{-1}). Between these end-member values we capture the wide range of fluid flow velocities summarized below. We acknowledge that the constraints imposed by this assumption are rough, however our model can be easily changed to accommodate better informed estimates.

4. Numerical Results

4.1. Porous Flow

[15] In the simplest case we assume that the liquid metal is interconnected and can flow through a permeable silicate matrix. This state of affairs corresponds to the textures preserved in the Kernouvé sample that has been heated above the melting point of Fe-Ni-S (T ~ 900°C at 1.0 GPa) but not deformed experimentally. In this sense the texture reflects a "control" state for slow (creeping) fluid flow and corresponds well to the earliest stages of melt segregation in planetesimal bodies subjected only to thermal stress. Darcy flow describes fluid flow driven by gradients in pressure. For steady state flow the governing equation is

$$\nabla \cdot \left[-\frac{\kappa}{\eta} \nabla \left(p_{dl} + \rho_f g D \right) \right] = Q_s, \qquad (1)$$

where k is the silicate matrix permeability (m^2), η is the dynamic viscosity, ρ_f the fluid density (kg m^{-3}), and g acceleration due to gravity. In the numerical scheme, D is the coordinate for vertical elevation, and Q_s is the volumetric flow rate per unit volume of reservoir for a fluid source. In the model D is set to zero as the elevation potential is negligible given the small scale of the sample under investigation.

[16] Figure 3 shows the recovered 2-D pressure field derived uniquely for the image-based mesh geometry shown in Figure 2 for a pressure gradient of 1.25 Pa m^{-1}. Melt streamlines and melt flow direction (arrows) are shown in red. The computed

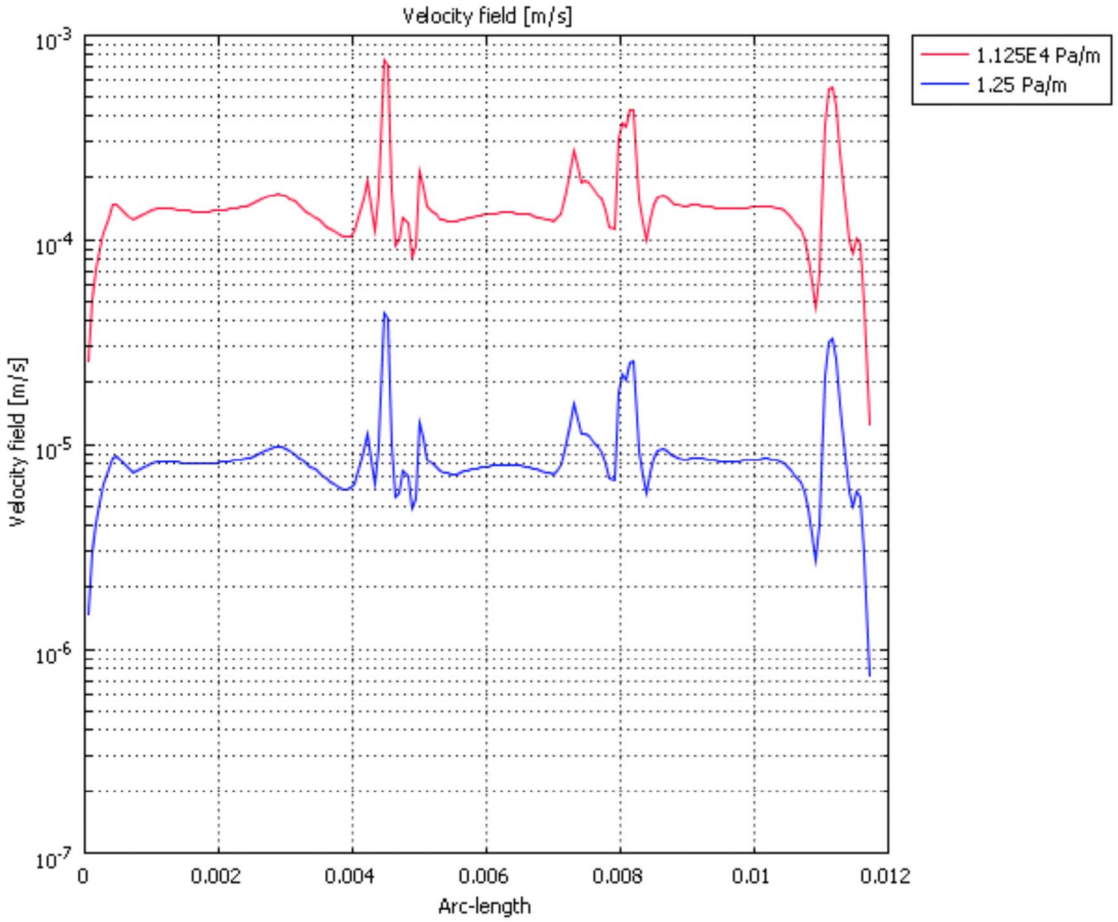

Figure 6. Two flow profiles showing effect of changing pressure gradient on melt flow velocities. A fourfold increase in pressure gradient from ~1 to 10^4 Pa m^{-1} results in an order of magnitude increase in Darcy flow velocity where the fluid properties remain constant. Matrix permeability is 10^{-10} $m^{2.}$

flow field gives an idea of the complex motions and pathways available to fluid particles as they migrate through the sample. The gray FeS metal domains seen in Figure 1 (the geometrical template to the model) represent quenched pockets of liquid metal that would have originally been molten. Assuming this is true for the simulation, a striking feature of the model is the deflection of melt percolating downward through the matrix toward and into the larger melt pockets where overall pressure is lower. Although not modeled, qualitatively it is possible that these sites will grow in size to a radius where in principle gravitational instabilities cause segregation via raining [e.g., *Stevenson*, 1990]. We elaborate on this point in section 5.

[17] Using the image-based modeling approach it is possible to estimate the fluid flow velocity as a function of matrix permeability and position within the sample image. Figure 4 shows the effect of variable matrix permeability on flow rate calculated in a line traverse across the mid point of the model (Figure 2). As expected, the fastest average migration velocities (~10^{-5} m s^{-1}) correspond with the largest permeability (10^{-10} m^2).

[18] We now examine the case where the pressure gradient is increased. Figure 5 shows a surface pressure plot where $\Delta P = 1.125 \times 10^4$ Pa m^{-1}. While the flow geometry remains similar to the previous model, the overall velocity increases markedly. This is seen more clearly in Figure 6, where the mean flow velocity increases from ~10^{-5} to 10^{-4} m s^{-1}.

4.2. Deformation-Induced Microsegregation

[19] The second set of numerical experiments makes use of the geometries and textures resulting from combined partial melting and deformation. The role of deformation is to set up differential stresses that lead to brittle failure and local fracturing of the silicate matrix. For this part of the analysis, we use the textural results from the Kernouvé deformation

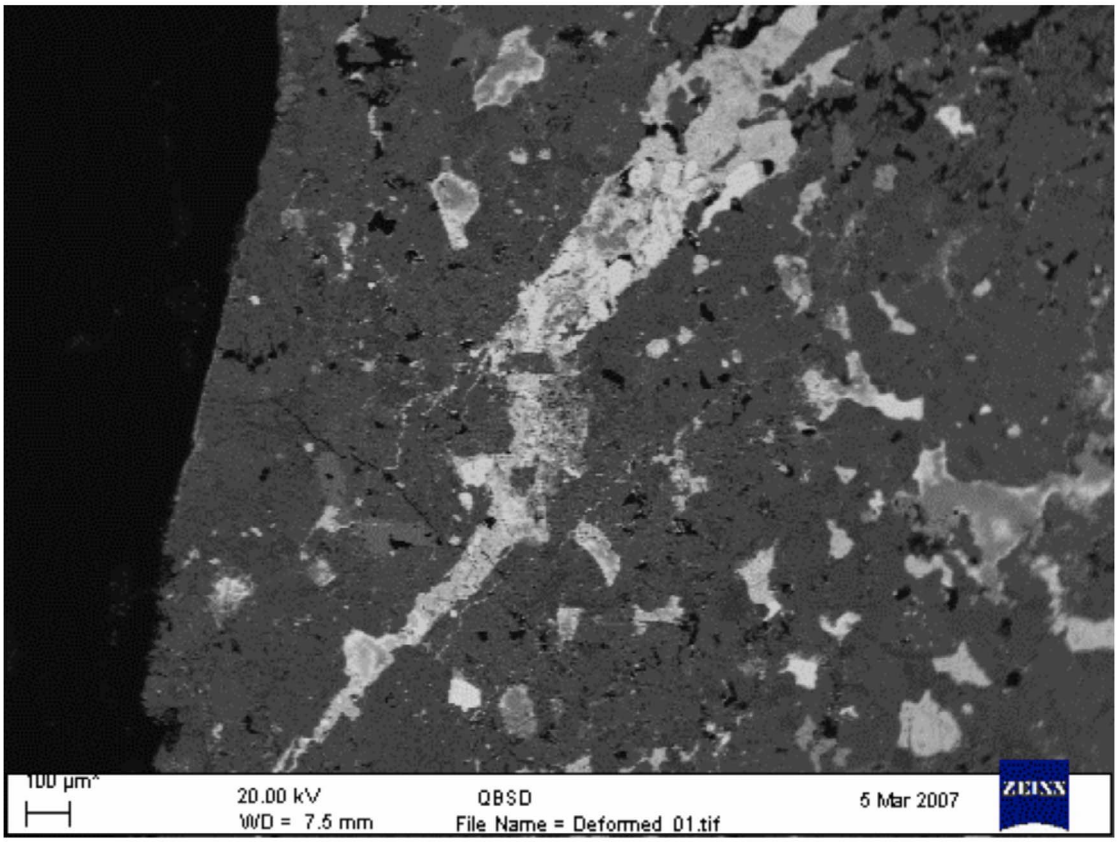

Figure 7. SEM image of a deformation-induced vein formed under laboratory conditions (sample KM 24, 940°C, 1.3 GPa, strain rate 10^{-4} s^{-1}). The texture contrasts with the undeformed natural sample shown in Figure 1, with FeS melt frozen into veins and pockets showing evidence of brittle deformation.

experiments, that is, the same H6 chondrite, but this time experimentally deformed. Deformation experiments were conducted on cores, 0.6″ long and 0.25″ in diameter using a Griggs rock deformation apparatus. Strain rates ranged between 10^{-4} s^{-1} and 10^{-6} s^{-1} at pressures in the range 1.0 to 1.3 GPa and temperatures between 900°C and 1000°C. The experimental details are given by *Rushmer et al.* [2000, 2005]. Textural observations and analyses show extensive evidence of focused zones of shear and fracture. These zones contain quenched Fe-Ni-S liquid and evidence of remobilized Fe-Ni metal. At higher temperatures (>940°C) when silicate melt is present, textures indicate that significant changes occur in surface energy relationships between liquid metal and silicate. The liquid metal phase becomes bleb-like in the presence of silicate melt and the sample no longer undergoes fracture at these strain rates.

[20] In the silicate melt-free samples, microscopic observations of the experimental charges show that liquid metal has moved preferentially into narrow veins and cracks that occur along grain boundaries or crosscut the granular matrix. In some regions of the sample (Figure 7) melt has collected in volume within larger veins oriented parallel to the direction of maximum compression. Observations on the collection and distribution of liquid metal melt in samples subjected to laboratory deformation are reported elsewhere and indicate that migration of small fractions of liquid metal can be driven by pressure gradients produced during deformation [*Groebner and Kohlstedt*, 2006; *Hustoft and Kohlstedt*, 2006]. Note also the potential for porous flow in the silicate matrix outside the larger vein structures. This remains an essential feature of the microsegregation processes modeled here. To do this we use a more sophisticated approach that couples simultaneously slow flow in the permeable silicate matrix with a Navier-Stokes solution for channel flow inside larger cracks and veins. A par-

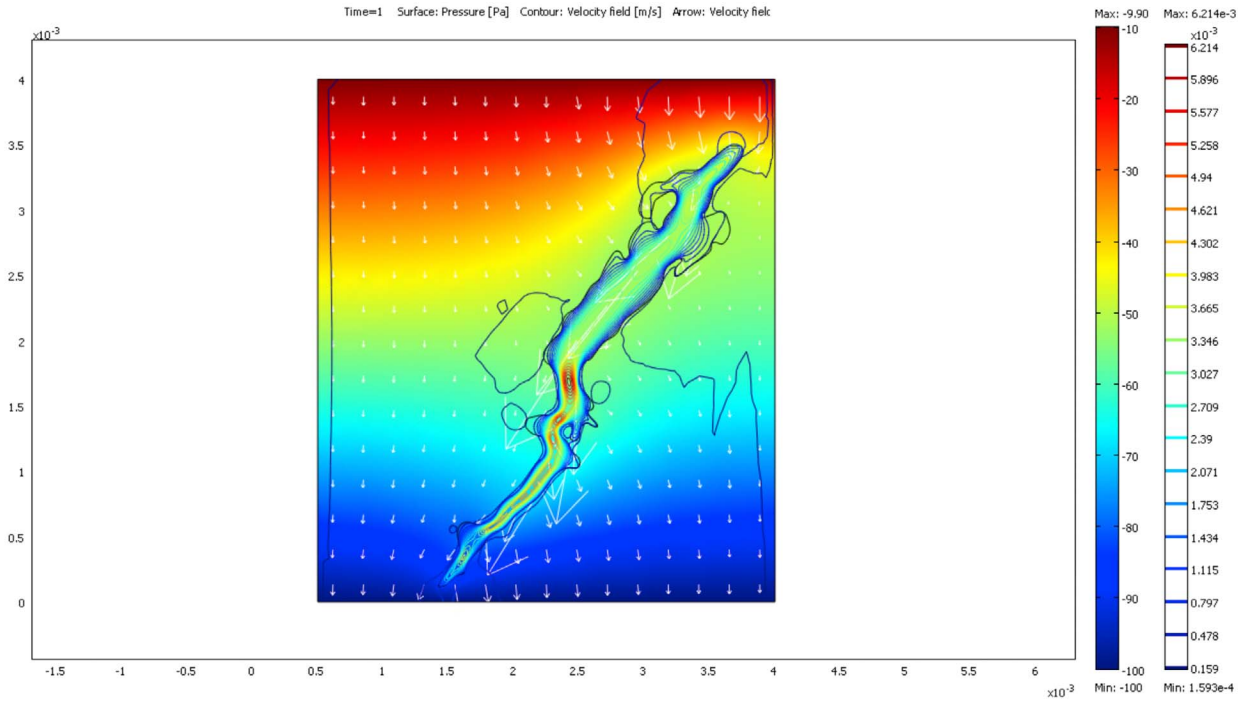

Figure 8. Plot of surface pressure gradient for vein texture shown in Figure 7. White arrows show the velocity field for a pressure gradient of 1.25 Pa m^{-1}. White arrows show the corresponding 2-D fluid flow field. Melt flow velocities range from ~10^{-4} to 10^{-3} m s^{-1} with highest velocities inside the vein.

ticular nuance in the model is that where fluid moves in a porous matrix but shear is nonnegligible, as is the case where melt approaches a larger open channel (vein) the Brinkman equations apply:

$$\left(-\nabla\cdot\eta\left(\nabla\mathbf{u}_{br}+(\nabla\mathbf{u}_{br})^{T}\right)\right)-\left(\frac{\eta}{k}\mathbf{u}_{br}+\nabla p_{br}-\mathbf{F}\right)=0$$
$$\nabla\cdot\mathbf{u}_{br}=0, \qquad (2)$$

where symbols and values are as in equation (1) and Table 2. Technically the permeability term k in the Brinkman equations differs slightly from k in Darcy's law but for ease of comparison we take here the same matrix permeability range and values in both. Finally we need to consider channel flow in the vein. Here we use the familiar Navier-Stokes equations, which combine a momentum balance with an equation of continuity via

$$-\nabla\cdot\eta\left(\nabla\mathbf{u}_{ns}+(\nabla\mathbf{u}_{ns})^{T}\right)+\rho(\mathbf{u}_{ns}\cdot\nabla)\mathbf{u}_{ns}+\nabla p_{ns}=0$$
$$\nabla\cdot\mathbf{u}_{ns}=0. \qquad (3)$$

[21] In the numerical solution scheme both the Brinkman and Navier-Stokes equations solve for dependent variables **u** and p. For the vein geometry discussed above, where liquid metal undergoing initial segregation via porous matrix flow moves toward a larger channel the interface to the Brinkman flow field is a velocity constraint such that the melt velocity just inside the vein is the same as that just outside it. Ensuring this continuity links the Navier-Stokes and Brinkman velocities and completes the model interface such that a numerical solution of the coupled flow field is achievable.

[22] Figure 8 shows the result of a simulation of the 2-D pressure field made using the geometry in Figure 7 for a ΔP of 1.25 Pa m^{-1}. Melt flow is shown as both streamlines and arrows (white) whose length is proportional to flow velocity. It is clear that while flow is taking place in the matrix away from the vein, melt here is moving at a substantially faster rate. Figure 9 is a compilation plot showing the simultaneous melt flow velocities across three cross sections (arc lengths) of the sample shown in Figure 7. Each velocity profile represents a slice through the sample from bottom (1) to top (3). The peaks correspond to flow inside the vein. The background (matrix) flow assumes a fixed permeability of 10^{-10} m^2. On average, liquid metal flow rates inside the vein (~10^{-4} m s^{-1}) are several orders of magnitude greater than background matrix flow. The effect of increasing pressure gradient on melt flow velocities is shown in Figure 10. Here two velocity profiles are plotted from the same midpoint position across the sample. Increasing the pressure

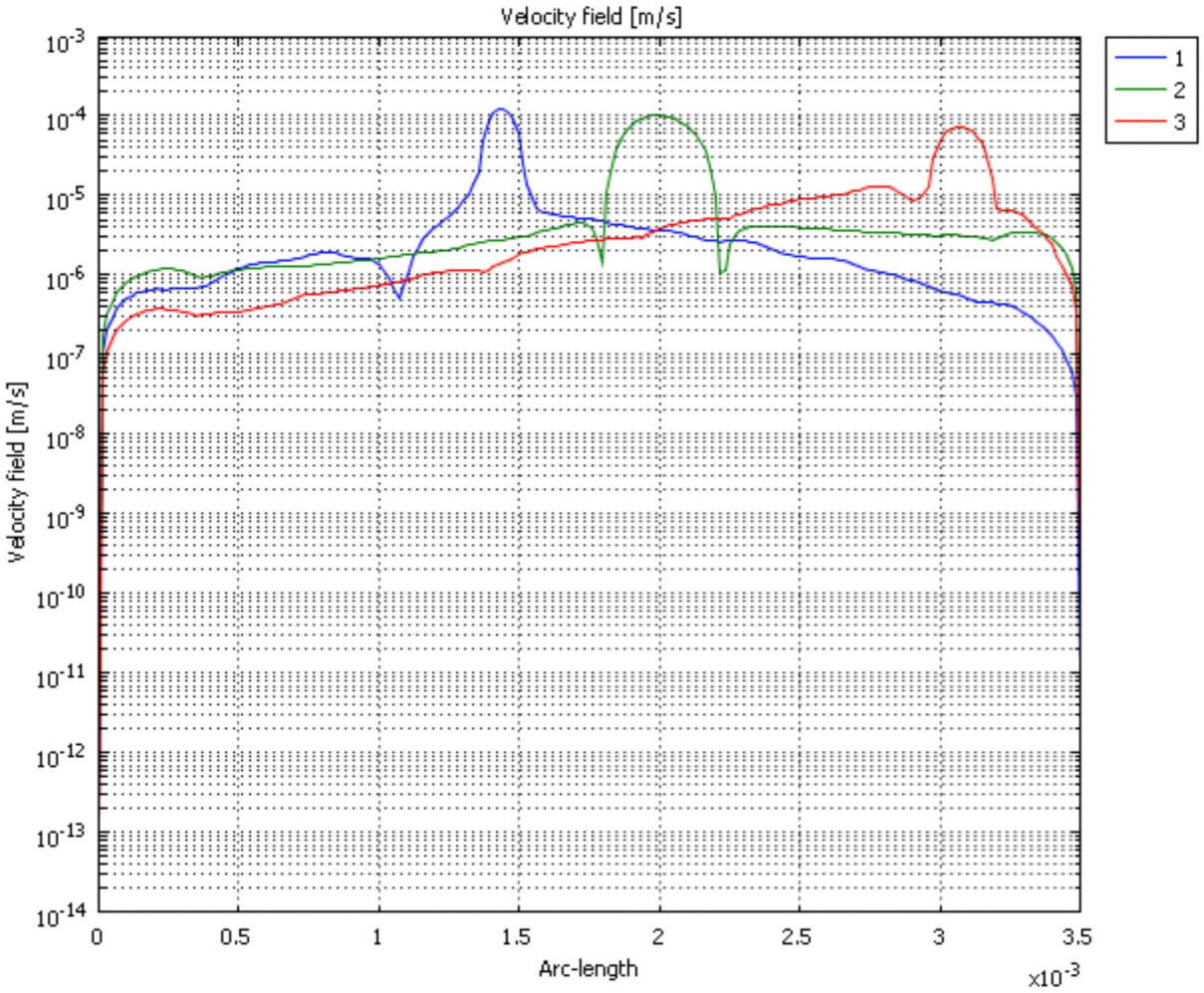

Figure 9. Coupled Brinkman-Navier-Stokes fluid flow model showing three melt velocity profiles across the deformed sample that intersect the vein at three positions: base (1), middle (2), and top (3). The vein is marked by distinct peaks in melt velocity profile. Pressure gradient is 1.25 Pa m^{-1}.

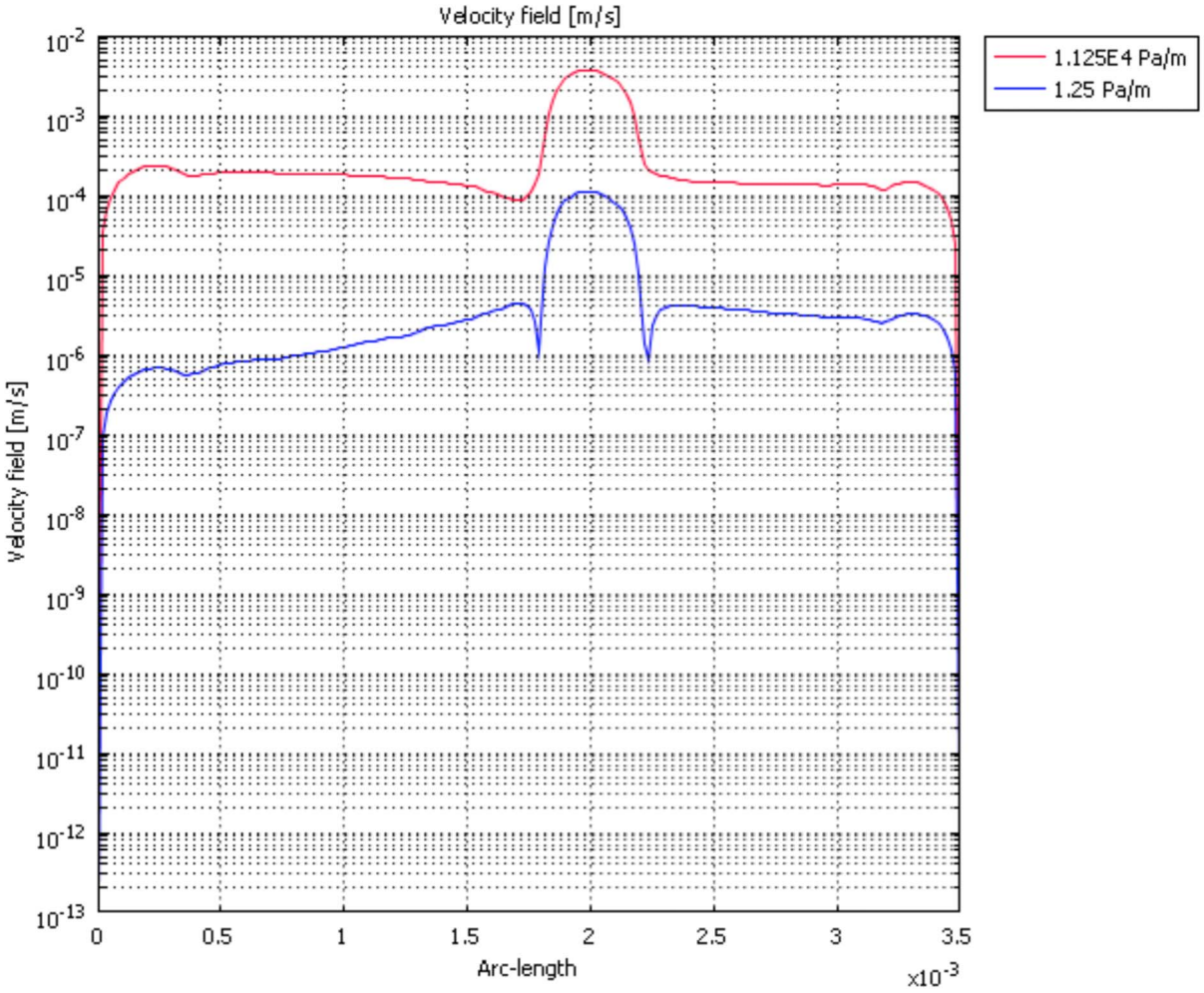

Figure 10. Two melt velocity profiles across the same midpoint position of veined sample as a function of pressure gradient and fixed matrix permeability of 10^{-10} m^2. Maximum predicted flow rates inside the vein exceed 1 mm s^{-1}.

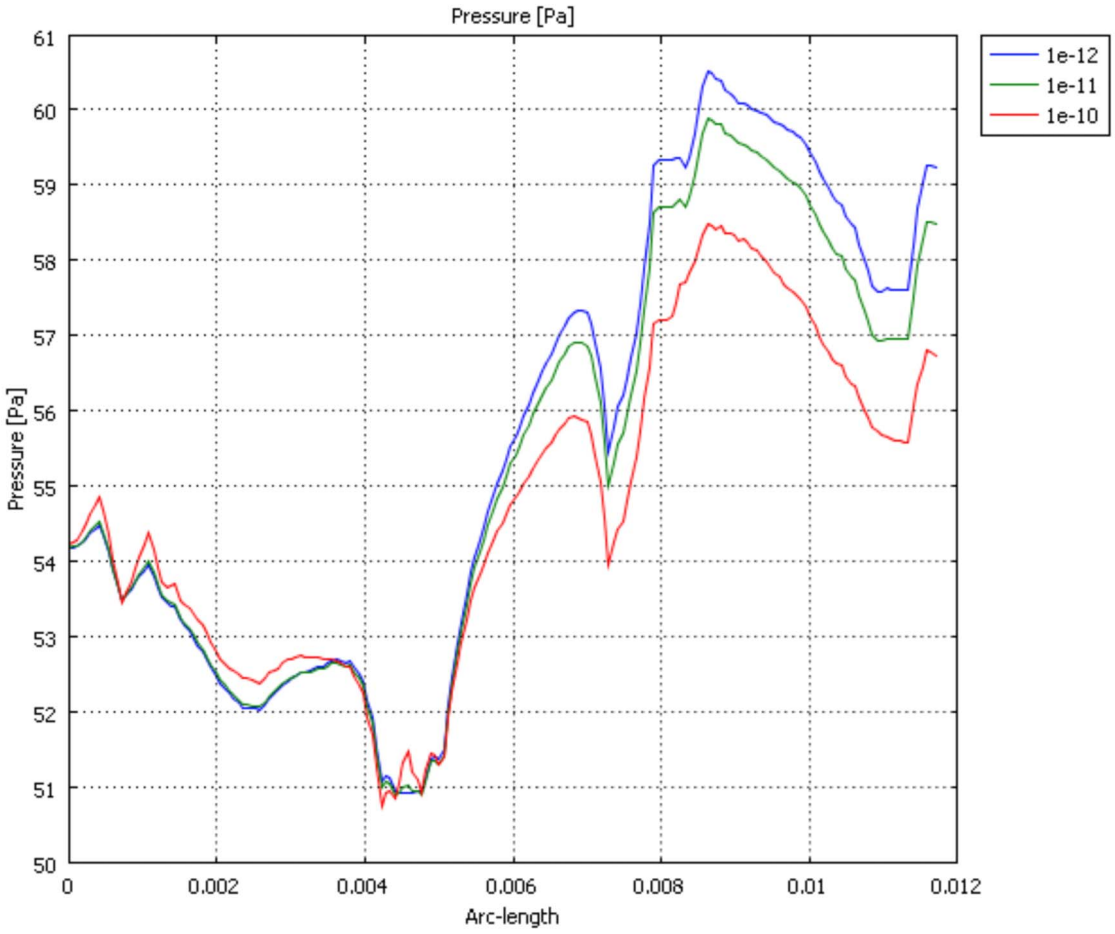

Figure 11. Three profiles showing fluctuations in fluid pressure (Pa) profile for matrix permeabilities in the range $10^{-12} < k < 10^{-10}$ m^2 at a fixed pressure gradient of 1.125×10^4 Pa m^{-1}.

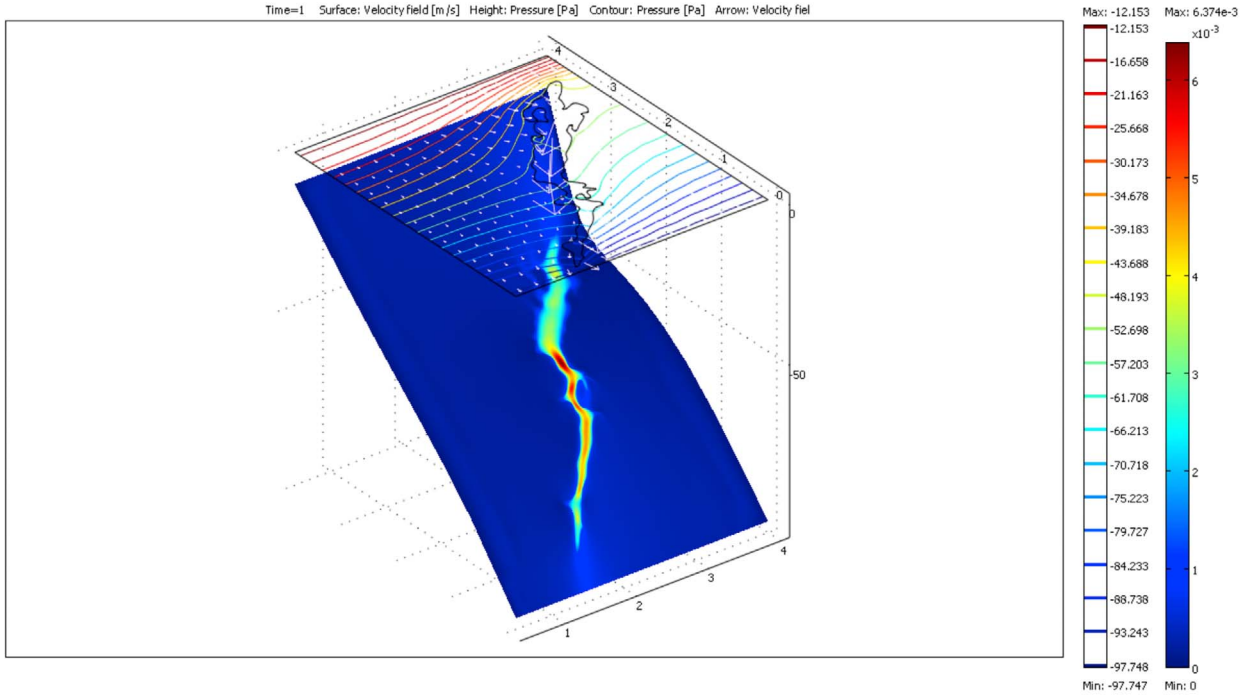

Figure 12. Summary compilation plot showing vein geometry surface pressure (contours) and melt flow velocity field (white arrows). Inclined image shows melt flow velocity field in and around the vein. Pressure gradient is 1.125×10^4 Pa m^{-1}.

gradient causes the flow velocity to increase in concert, but the effect is not a simple linear increase. The maximum flow velocity inside the vein is ~5×10^{-3} m s^{-1} (5 mm s^{-1}) for a pressure gradient of 1.125×10^4 Pa m^{-1}. It is interesting to note for completeness that the melt pressure is also position dependent within the sample and decreases with increasing matrix permeability (Figure 11). Finally, it is possible to combine several 2-D surface plots such that the vein geometry, fluid velocity and pressure fields can be visualized simultaneously (Figure 12).

[23] In summary, and erring on the side of caution (assuming a lower pressure gradient is more realistic), then comparison of both model geometries shows that all being equal microsegregation by flow in veins is a factor of 10 faster than porous flow as modeled in the undeformed case. These results are however highly dependent on the exact choice of matrix permeability.

5. Discussion

[24] While we have not sought to address the larger scale issue of planetary core formation in our analysis of microsegregation rates, this work is nonetheless amenable to upscaling, with implications for metal liquid segregation in a solid silicate matrix beneath for example an early magma ocean [*Stevenson*, 1990; *Walter and Tronnes*, 2004]. Here, aided by deformation, microsegregation via Darcy flow or flow in veins could help feed accumulations of metal that then become unstable and sink as diapirs. It is noteworthy that *Yoshino et al.* [2003, 2004] were not the first to use Darcy's law to approximate liquid metal transport times in silicate bodies; *Stevenson* [1981], citing *Walker et al.* [1978] discussed this approach several decades earlier.

[25] In the first stages of microsegregation (which these models address specifically), liquid metal flow rates may be rapid. For a 100 km radius planetesimal, *Yoshino et al.* [2003] predicted a transit time from surface to core of < 600 years while *Rushmer et al.* [2005] using a dilatancy model, calculated potential liquid metal flow rates of $<10^{-4}$ m s^{-1}. In this study, we find that potential melt flow rates, scaled to a 100 km diameter body, indicate that liquid metal could travel this distance in as little as 30 years providing flow is continuous and through veins. Within an order of magnitude these numerical values are within current best estimates of core formation based on isotopic analysis (<1.5 Ma). It is an interesting open question whether isotopic methods will ever be sensitive enough to confirm

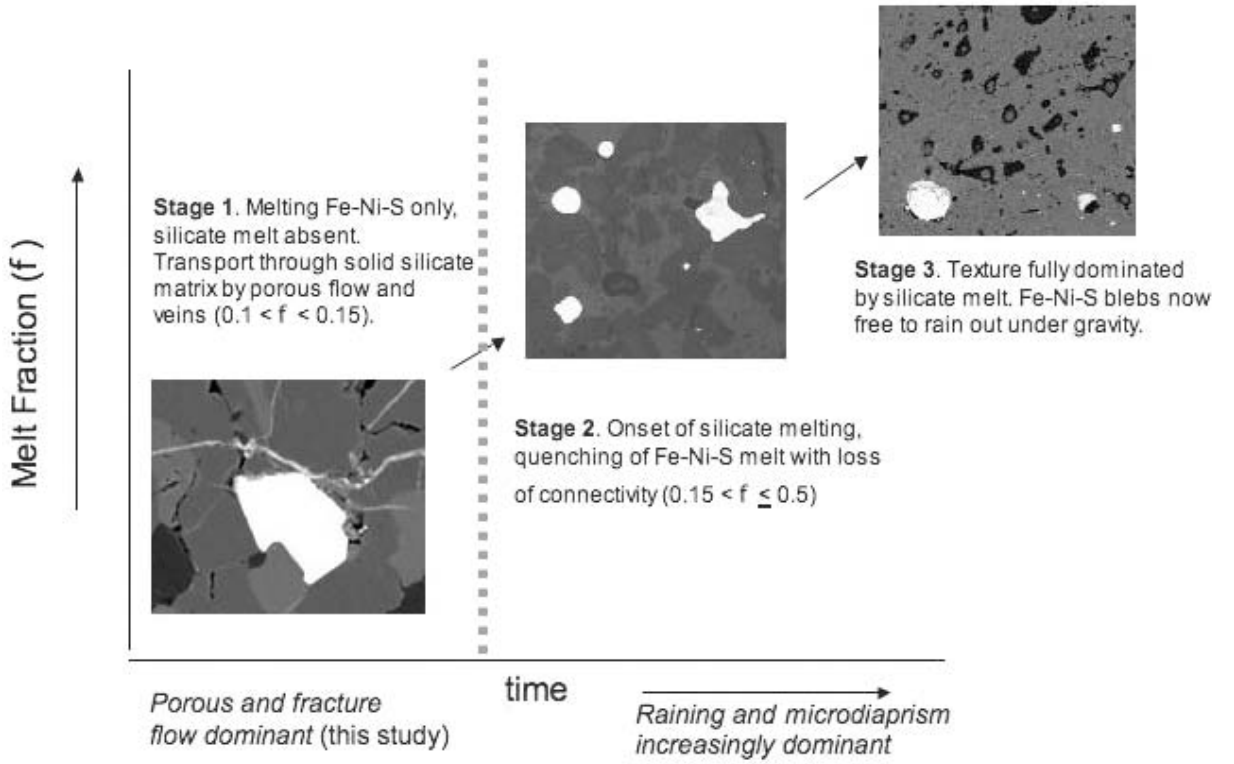

Figure 13. Proposed three-stage process of liquid metal microsegregation as a function of melt fraction based on textural analysis of Kernouvé H6 chondite during progressive partial melting. The numerical results of this study apply to stage 1 only. Here *f* indicates melt fraction.

the rapid core formation times implied by physical models where matrix permeability permits rapid extraction. The timeframe will change however where permeability is small. For example, the matrix permeabilites suggested by *Bagdassarov et al.* [2009] would reduce liquid metal segregation rates by porous flow alone significantly. Clearly more work is needed to better constrain this important parameter in undeformed systems but we note (as shown here) that where flow takes place primarily in veins, the exact value of matrix permeability is unlikely to be a constraining factor.

[26] Although not addressed specifically in this numerical study, another important consideration is the role of silicate melt. Additional experiments on Kernouvé at high temperatures show that quench liquid metal in the presence of silicate melt all have spherical bleb shapes (beads) when found in contact with the silicate melt [*Rushmer et al.*, 2000]. These types of textures were also discussed by *Yoshino et al.* [2004] and *Hustoft and Kohlstedt* [2006]. Once silicate melt is present, there is no evidence of extensive localized shearing and deformation is distributed. The presence of silicate melt would appear to shut off porous flow in these systems. Therefore, interconnectivity breaks down at a critical threshold defined by onset of silicate melting, implying a different physical mechanism must take over for efficient metal-silicate separation to occur. We summarize how we see the progression in segregation mechanisms as a function of increasing temperature in Figure 13.

6. Summary

[27] We have presented the initial results of an image-based numerical model aimed at quantifying liquid metal microsegregation rates during the earliest stages of partial melting in silicate Ni-Fe systems. Our results using both natural and experimental textures show that during porous flow, metallic liquid can be drawn into high-permeability and low-pressure sites of initial melting and that the liquid flow velocity is position dependent. Modifying the matrix permeability shows that the highest average liquid metal migration velocities (10^{-5} m s^{-1}) correspond to the largest model permeabilities (in this case 10^{-10} m^2). Our results follow those predicted by *Stevenson* [1989] that melt (metallic liquid) percolating through a porous matrix is drawn into

high-permeability, low-pressure sites of initial melting. When deformation textures are included in the modeling, channel (vein) flow becomes important and we predict that most liquid metal will move through deformation-induced veins or cracks. Depending upon the driving pressure gradient, average melt flow velocities are of the order 10^{-4} to 10^{-3} m s^{-1}. The implication is that deformation can enhance by several orders of magnitude the melt flow velocities, and hence overall segregation rates of liquid metal from silicate matrix. However, the "window of opportunity" for liquid metal segregation is limited by the production of silicate melt as melting intensifies. The effect of silicate melt is to effectively close down porous flow of liquid metal and marks a threshold where gravitational settling becomes the dominant microsegregation mechanism.

Acknowledgments

[28] TR acknowledges DP 0986232 from the Australian Research Council and MQRDG from Macquarie University. NP would like to thank David Wertheim, N. Upton, and V. Lewis (Kingston University) and acknowledge NERC grant NE/F01080X/1. We thank two anonymous reviewers for helpful and clear reviews that improved the paper. This is GEMOC publication 700.

References

Bagdassarov, N., G. Solfernio, G. J. Golbeck, and M. W. Schmidt (2009), Centrifuge assisted percolation of Fe-S melts in partially molten peridotite: Time constraints for planetary core formation, *Earth Planet. Sci. Lett.*, *288*, 84–95, doi:10.1016/j.epsl.2009.09.010.

Ballhaus, C., and D. J. Ellis (1996), Mobility of core melts during Earth's accretion, *Earth Planet. Sci. Lett.*, *143*, 137–145, doi:10.1016/0012-821X(96)00135-5.

Bruhn, D., N. Groebner, and D. L. Kohlstedt (2000), An interconnected network of core-forming melts produced by shear deformation, *Nature*, *403*, 883–886, doi:10.1038/35002558.

Burkhardt, C., T. Kleine, B. Bourdon, H. Palme, J. Zipfel, J. M. Friedrich, and D. S. Ebel (2008), Hf-W mineral isochron for Ca,Al-rich inclusions: Age of the solar system and the timing of core formation in planetesimals, *Geochim. Cosmochim. Acta*, *72*, 6177–6197, doi:10.1016/j.gca.2008.10.023.

Carlson, R. W., and M. Boyet (2009), Short-lived radionuclides as monitors of early crust–mantle differentiation on the terrestrial planets (Frontiers), *Earth Planet. Sci. Lett.*, *279*, 147–156, doi:10.1016/j.epsl.2009.01.017.

Chen, S., Z. Q. Yue, and L. G. Tham (2004), Digital image-based numerical modeling method for prediction of inhomogeneous rock failure, *Int. J. Rock Mech. Min. Sci.*, *41*, 939–957.

Groebner, N., and D. L. Kohlstedt (2006), Deformation-induced metal melt networks in silicates: Implications for core–mantle interactions in planetary bodies, *Earth Planet. Sci. Lett.*, *245*, 571–580, doi:10.1016/j.epsl.2006.03.029.

Harper, C. L., and S. B. Jacobsen (1996), Evidence for ^{182}Hf in the early solar system and constraints on the timescale of terrestrial core formation, *Geochim. Cosmochim. Acta*, *60*, 1131–1153, doi:10.1016/0016-7037(96)00027-0.

Hustoft, J. W., and D. L. Kohlstedt (2006), Metal-silicate segregation in deforming dunitic rocks, *Geochem. Geophys. Geosyst.*, *7*, Q02001, doi:10.1029/2005GC001048.

Jarosewich, E. (1990), Chemical analyses of meteroites: A compilation of stony and iron meterorite analyses, *Meteoritics*, *25*, 323–337.

Kelly, W. R., and G. J. Wasserburg (1978), Evidence for the existence of ^{107}Pd in the early solar system, *Geophys. Res. Lett.*, *5*, 1079–1082, doi:10.1029/GL005i012p01079.

Kleine, J., K. Munker, K. Meztger, and H. Palme (2002), Rapid accretion and early core formation on asteroids and the terrestrial planets from Hf–W chronometry, *Nature*, *418*, 952–955, doi:10.1038/nature00982.

Kleine, T., K. Mezger, H. Palme, E. Scherer, and C. Munker (2005), Early core formation in asteroids and late accretion of chondrite parent bodies: Evidence from ^{182}Hf–^{182}W in CAIs, metal-rich chondrites, and iron meteorites, *Geochim. Cosmochim. Acta*, *69*, 5805–5818, doi:10.1016/j.gca.2005.07.012.

Kleine, T., M. Touboul, J. A. Van Orman, B. Bourdon, C. Maden, K. Mezger, and A. N. Halliday (2008), Hf-W thermochronometry: Closure temperature and constraints on the accretion and cooling history of the H chondrite parent body, *Earth Planet. Sci. Lett.*, *270*, 106–118, doi:10.1016/j.epsl.2008.03.013.

Kleine, T., M. Touboul, B. Bourdon, F. Nimmo, K. Mezger, H. Palme, S. B. Jacobsen, Q.-F. Yin, and A. N. Halliday (2009), Hf–W chronology of the accretion and early evolution of asteroids and terrestrial planets, *Geochim. Cosmochim. Acta*, *73*, 5150–5188, doi:10.1016/j.gca.2008.11.047.

Lee, D.-C. (2005), Protracted core formation in asteroids: Evidence from high precision W isotopic data, *Earth Planet. Sci. Lett.*, *237*, 21–32, doi:10.1016/j.epsl.2005.06.033.

Lee, D.-C., and A. N. Halliday (1995), Hafnium–tungsten chronometry and the timing of terrestrial core formation, *Nature*, *378*, 771–774, doi:10.1038/378771a0.

Lee, D.-C., and A. N. Halliday (1996), Hf–W isotopic evidence for rapid accretion and differentiation in the early solar system, *Science*, *274*, 1876–1879, doi:10.1126/science.274.5294.1876.

Markowski, A., G. Quitte, A. N. Halliday, and T. Kleine (2006), Tungsten isotopic compositions of iron meteorites: Chronological constraints vs. cosmogenic effects, *Earth Planet. Sci. Lett.*, *242*, 1–15, doi:10.1016/j.epsl.2005.11.048.

Minarik, W. G., F. J. Ryerson, and E. B. Watson (1996), Textural entrapment of core-forming melts, *Science*, *272*, 530–533, doi:10.1126/science.272.5261.530.

Petford, N., T. Rushmer, and G. Lansdown (2006), Numerical modelling of liquid metal transport in molten H6 ordinary chondrite, *Lunar Planet. Sci.*, *XXXVII*, Abstract 1603.

Qin, L., N. Dauphas, M. Wadhwa, J. Masarik, and P. E. Janney (2008), Rapid accretion and differentiation of iron meteorite parent bodies inferred from ^{182}Hf–^{182}W chronometry and thermal modeling, *Earth Planet. Sci. Lett.*, *273*, 94–104, doi:10.1016/j.epsl.2008.06.018.

Quitté, G., M. Meier, C. Latkoczy, A. N. Halliday, and D. Günther (2006), Nickel isotopes in iron meteorites–nucleosynthetic anomalies in sulphides with no effects in

metals and no trace of ^{60}Fe, *Earth Planet. Sci. Lett.*, *242*, 16–25, doi:10.1016/j.epsl.2005.11.053.

Roberts, J. J., J. Siebert, F. J. Ryerson, and J. H. Kinney (2007), Fe-Ni-S melt permeability in olivine: Implications for planetary core formation, *Geophys. Res. Lett.*, *34*, L14306, doi:10.1029/2007GL030497.

Rubin, A. E. (2003), Chromite-Plagioclase assemblages as a new shock indicator; implications for the shock and thermal histories of ordinary chondrites, *Geochim. Cosmochim. Acta*, *67*, 2695–2709, doi:10.1016/S0016-7037(03)00107-8.

Rushmer, T., W. G. Minarik, and G. J. Taylor (2000), Physical processes of core formation, in *Origin of the Earth and Moon*, edited by R. M. Canup and K. Righter, pp. 227–245, Univ. of Ariz. Press, Tuscon.

Rushmer, T., B. Zanda, and M. Bourot-Denise (2002), Experimental deformation of ordinary chondrite under partially molten conditions: Application to natural samples and implications for early differentiation processes, *Lunar Planet. Sci.* [CD-ROM], XXXII, Abstract 1706.

Rushmer, T., N. Petford, M. Humayun, and A. J. Campbell (2005), Fe-liquid segregation in deforming planetesimals: Coupling Core-Forming compositions with transport phenomena, *Earth Planet. Sci. Lett.*, *239*, 185–202, doi:10.1016/j.epsl.2005.08.006.

Secco, R. A., G. E. LeBlanc, H. Yang, and J. N. Seibel (1998), High pressure viscosity of an Fe-S liquid: Experimentally derived of the viscosity of the outer earth's core, in *Properties of Earth and Planetary Materials at High Pressure and Temperature*, *Geophys. Monogr. Ser.*, vol. 101, edited by M. H. Manghanani and T. Yagi, pp. 495–506, AGU, Washington D. C.

Shannon, M. C., and C. B. Agee (1996), High pressure constraints on percolative core formation, *Geophys. Res. Lett.*, *23*, 2717–2720, doi:10.1029/96GL02817.

Stevenson, D. J. (1981), Models of the Earth's core, *Science*, *214*, 611–619, doi:10.1126/science.214.4521.611.

Stevenson, D. J. (1989), Spontaneous small-scale melt segregation in partial melts undergoing deformation, *Geophys. Res. Lett.*, *16*, 1067–1070, doi:10.1029/GL016i009p01067.

Stevenson, D. J. (1990), Fluid dynamics of core formation, in *The Origin of the Earth*, edited by H. Newsom and J. H. Jones, pp. 231–249, Oxford Press, London.

Stoeffler, D., K. Keil, and E. R. D. Scott (1991), Shock metamorphism of ordinary chondrites, *Geochim. Cosmochim. Acta*, *55*, 3845–3867, doi:10.1016/0016-7037(91)90078-J.

Terasaki, H., T. Kato, S. Urakawa, K. Funakoshi, A. Suzuki, T. Okada, M. Maeda, J. Sato, T. Kubo, and S. Kasai (2001), The effect of temperature, pressure, and sulfur content on viscosity of the Fe-FeS melt, *Earth Planet. Sci. Lett.*, *190*, 93–101, doi:10.1016/S0012-821X(01)00374-0.

Walker, D., E. M. Stolper, and J. F. Hayes (1978), A numerical treatment of melt/solid segregation: Size of the Eucrite parent body and stability of the terrestrial low-velocity zone, *J. Geophys. Res.*, *83*, 6005–6013, doi:10.1029/JB083iB12p06005.

Walter, M. J., and R. G. Tronnes (2004), Early earth differentiation, *Earth Planet. Sci. Lett.*, *225*, 253–269, doi:10.1016/j.epsl.2004.07.008.

Wlotzka, F. (1993), A weathering scale for the ordinary chondrites, *Meteoritics*, *28*, 460.

Xiaobin, S., G. Narsilio, Hongxin Wang, D. Smith, and G. Egan (2007), Using numerical model to predict hydrocephalus based on MRI images, paper presented at Joint Meeting of the 6th International Symposium on Noninvasive Functional Source Imaging of the Brain and Heart and the International Conference on Functional Biomedical Imaging, Inst. of Electr. and Electron. Eng., Hangzhou, China.

Yin, Q., S. B. Jacobsen, K. Yamashita, J. Blichert-Toft, P. Telouk, and F. Albarede (2002), A short timescale for terrestrial planet formation from Hf-W chronometry of meteorites, *Nature*, *418*, 949–952, doi:10.1038/nature00995.

Yoshino, T., M. J. Walter, and T. Katsura (2003), Core formation in planetesimals triggered by permeable flow, *Nature*, *422*, 154–157, doi:10.1038/nature01459.

Yoshino, T., M. J. Walter, and T. Katsura (2004), Connectivity of molten Fe alloy in peridotite based on in situ electrical conductivity measurements: Implications for core formation in terrestrial planets, *Earth Planet. Sci. Lett.*, *222*, 625–643, doi:10.1016/j.epsl.2004.03.010.